

# Dark Matter in Dwarf Spheroidals II: Observations and Modelling of Draco

J. Kleyna<sup>1</sup>, M.I. Wilkinson<sup>1</sup>, N.W. Evans<sup>2</sup>, G. Gilmore<sup>1</sup>

<sup>1</sup> *Institute of Astronomy, Madingley Rd, Cambridge CB3 0HA*

<sup>2</sup> *Theoretical Physics, Department of Physics, 1 Keble Road, Oxford, OX1 3NP*

## ABSTRACT

We present stellar radial velocity data for the Draco dwarf spheroidal (dSph) galaxy obtained using the AF2/WYFFOS instrument combination on the William Herschel Telescope. Our dataset consists of 186 member stars, 159 of which have good quality velocities, extending to a magnitude  $V \approx 19.5$  with a mean velocity precision of  $\approx 2 \text{ km s}^{-1}$ . As this survey is based on a high-precision photometric target list, it contains many more Draco members at large radii. For the first time, this allows a robust determination of the radial behaviour of the velocity dispersion in a dSph.

We find statistically strong evidence of a rising velocity dispersion consistent with a dark matter halo with gently rising rotation curve. There is a  $< 2\sigma$  signature of rotation about the long axis, inconsistent with tidal disruption being the source of the rising dispersion. By comparing our dataset with earlier velocities, we find that Draco probably has a binary distribution and fraction comparable to those in the solar neighbourhood.

We apply a novel maximum likelihood algorithm and fit the velocity data to a two parameter spherical model with an adjustable dark matter content and velocity anisotropy. Draco is best fit by a weakly tangentially anisotropic distribution of stellar orbits in a dark matter halo with a very slowly rising rotation law ( $v_{\text{circ}} \propto r^{0.15}$ ). We are able to rule out both a mass-follows-light distribution and an extended halo with a harmonic core at the 2.5 to  $3\sigma$  significance level, depending on the details of our assumptions about Draco's stellar binary population. Our modelling lends support to the idea that the dark matter in dwarf spheroidals is distributed in the form of massive, nearly isothermal haloes.

**Key words:** galaxies: individual: Draco – galaxies: kinematics and dynamics – Local Group – dark matter – celestial mechanics, stellar dynamics

## 1 INTRODUCTION

This paper describes observations and dynamical modeling of the Draco dwarf spheroidal (dSph) galaxy. Draco was the first dSph with evidence of a large dark matter content. Aaronson (1983) measured the velocities of four carbon stars in Draco, inferring a mass far larger than that corresponding to Draco's visible matter. Subsequently, Aaronson & Olszewski (1987, 1988) obtained the velocities of  $\sim 15$  more stars and computed a velocity dispersion of  $\sim 10 \text{ km s}^{-1}$  and a mass-to-light ratio of  $> 50 M_{\odot}/L_{\odot}$ . These results were confirmed by a much larger sample of 91 Draco stars by Armandroff, Olszewski, & Pryor (1995, hereafter AOP), and 17 largely overlapping stars observed by Hargreaves et al. (1996). Lokas (2001) found that the dispersion profile of the inner part of Draco is consistent with standard CDM halo models, but core data alone cannot rule out mass-follows-light. These studies yielded velocity dispersions of  $8.5$  and  $10.5 \text{ km s}^{-1}$  respectively. The corresponding mass-to-light ratios, assuming the standard mass-follows-light King model (e.g., Binney & Tremaine, chap. 4), were  $90 \pm 15$  and  $145_{-71}^{+116}$

respectively.

However, these calculations depend on the assumption of a mass-follows-light King model. All the evidence from galactic dynamics is that dark matter does not trace the luminous mass but exists in extended halos (see e.g., Binney & Tremaine 1987, chap. 10). Also, the King model assumes isotropic orbits and this assumption hides the well-known degeneracy between mass and anisotropy. A tangentially anisotropic system, with orbits that become more circular with increasing radius, may have a velocity dispersion that rises with radius, effectively mimicking a massive halo.

In Sections 2 and 3 of the paper, we present the first Draco velocity data at projected radii significantly outside the King core radius. As our initial target list is based on accurate CCD data, rather than photographic plate photometry, we are able to achieve a clean separation between Draco's giant branch population and the Galactic foreground out to distances as large as Draco's nominal tidal radius. Consequently, these data contain many more stars at large radii than previous studies. At projected radii  $R > 10'$  (approximately the King core radius), our sample

has 63 stars, whereas the dataset of AOP contains 13. At  $R > 20'$ , our dataset contains 13 stars, compared to only one star in AOP. Furthermore, advances in instrumentation have made the velocities of our dataset more accurate than those previously published: our mean velocity uncertainty is  $1.9 \text{ km s}^{-1}$ , whereas the mean uncertainties of AOP and Hargreaves et al. (1996) were 3.1 and  $\gtrsim 2 \text{ km s}^{-1}$  respectively. In Section 4, we compare the velocities of stars in our dataset with the previous data set of AOP and use the disagreement between the two to constrain Draco’s binary fraction.

Section 5 presents the dynamical modelling of the data. As an advance beyond the standard mass-follows-light King models, we use a set of spherically symmetric dSph models described in our companion paper (Wilkinson et al. 2001, hereafter Paper I). The models have two free parameters, the first being the orbital anisotropy and the second being the dark matter content. Some care is needed in comparing the models to the data, as we must incorporate the effects of binary stars on the velocity dispersion, as well as uncertainties in the measurements. Our model fitting represents the first attempt to probe the spatial nature of a dSph dark matter halo and to disentangle the effects of halo mass from those of orbital anisotropy.

## 2 DATA

Data were obtained from June 23 to June 26, 2000, at the William Herschel Telescope using the AF2/WYFFOS fibre-fed spectrograph. Sky conditions were excellent over all four nights and no time was lost to weather or instrument difficulties. The one degree field of view of this instrument is well-matched to the King tidal radius of Draco, permitting all fields to be positioned on the same point at the centre of Draco. Typically, approximately 60 to 70 of the 101 functioning fibres could be placed on target stars. Most of the remaining fibres were allocated to sampling the sky spectrum. Two fibre configurations were observed per night. Typically, half an hour was lost to the intervening fibre reconfiguration. Usually, approximately seven fields were obtained for each arrangement of fibres. Fibres were re-allocated in a manner that attempted to achieve comparable signal-to-noise ( $S/N$ ) for each star regardless of magnitude. Stars that are near the centre of Draco, or that had been observed previously by other groups, were given a decreased weight when allocating fibres. Nevertheless, 62 of our final member stars have previous velocity measurements.

Stars were selected from a prior  $V$  and  $I$  band CCD survey of Draco, obtained with the 1.2m telescope at the Fred Lawrence Whipple Observatory. The 406 targets were chosen by selecting stars inside a polygon tightly drawn around the giant branch branch, spanning a magnitude range of  $V \approx 17$  to  $V \approx 19.8$ . The relatively good quality of the CCD photometry used to compile the target list, compared to the plate based photometry used as a basis for previous radial velocity observations, allowed a high yield of member stars out to Draco’s tidal radius. A total of 284 stars were observed, 203 of which had good-quality velocities and 186 of which proved to be probable Draco members. Figure 1 shows the positions of observed stars, superimposed on the core and tidal radii of Draco; open circles indicate members, plus symbols indicate probable members with low-quality

spectra, and dots indicate non-members.

The spectral range observed covered 8200 to 8800 Å, corresponding to the calcium triplet absorption line. Observations were performed using the ‘echelle’ grating with a resolution of 0.6 Å per pixel. Arc exposures using the ArNe lamp were taken every hour, so that each exposure was adjacent to at least one arc. Additionally, twilight skies were taken each evening and morning to obtain a velocity zero point using the solar spectrum.

## 3 DATA REDUCTION

Initial data reduction was performed using the WYFFOS-specific WYFFRED package inside IRAF. WYFFRED first identifies the traces of individual spectra on the chip using a bright reference image. Next, it fits scattered light from the image with a product of 11th and 3rd order Chebyshev polynomials, along and across the dispersion direction respectively. WYFFRED then uses the IDENTIFY task to dispersion-correct the spectra. For our spectra, a typical wavelength solution involved fitting 21 lines from the ArNe arc spectra with a fourth degree Chebyshev polynomial. Typically, the median scatter was  $0.02\text{Å}$ , corresponding to  $0.7 \text{ km s}^{-1}$ . The wavelength calibration was extremely stable through the night. Hence, each object exposure was calibrated using only its nearest-neighbour arc exposure rather than with a linear combination of the two adjacent arc exposures.

### 3.1 Sky Subtraction

The region of sky corresponding to the calcium triplet is very heavily contaminated by sky emission lines. The redmost line of the triplet, at 8662 Å, is masked by a complex of sky lines and was removed from the analysis altogether. The other two lines (at 8498 and 8542 Å) are immediately adjacent to strong sky lines. Thus, accurate sky subtraction is extremely important to obtain a symmetric peak in the cross-correlation of the object spectra with the template spectrum.

WYFFOS generates a composite sky spectrum for each exposure by computing the mean of the spectra of the sky fibres, rejecting those spectra that produce an excessive  $\chi^2$ . Next, it uses relative fibre throughputs obtained from a specially designated exposure to subtract the appropriate sky component from each individual object spectrum. For this work, the standard procedure was modified slightly to use the median of five throughput images rather than a single image, in case a star should lie on a fibre in one of the throughput images.

In theory (see e.g., Wyse & Gilmore 1992), this procedure should result in sky subtraction accurate to within one per cent. In the majority of cases, a good result was obtained. The residual of the sky lines was approximately symmetrical about a mean of zero, indicating that only the random Poisson noise element of the sky line remained and that the mean component had been correctly subtracted. Nevertheless, probably for reasons of non-Gaussian error contributions, the relative fibre throughput was sometimes miscalculated, resulting in incorrect sky subtraction and residual systematic sky line contamination. Because the sky lines contained of the order of  $10^3$  to  $10^4$  counts per pixel, even a very small systematic miscalculation of the sky could result

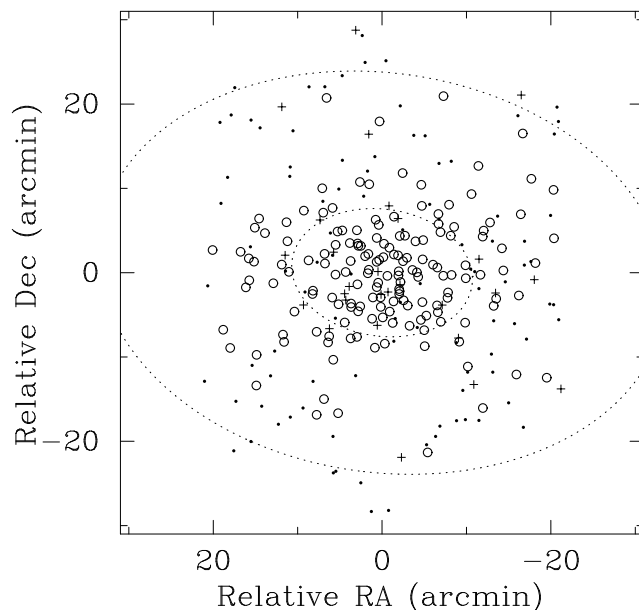


**Figure 1.** Locations of observed members with good velocities (open circles), probable members with low-quality velocities (plus symbols) and non-members (dots). Inner and outer ellipses are the King core and tidal radii, as deduced from a fit to the stellar surface number density (Irwin & Hatzidimitriou 1995).

in residual sky lines large relative to the Ca absorption lines. This residual contamination was removed using a bootstrap procedure that is described in the next subsection.

### 3.2 Combining Spectra

WYFFOS creates a set of multifibre spectra, each corresponding to a single exposure. Before cross-correlating the spectra with the template, it is thus necessary to split each multifibre spectrum into its constituent one-dimensional spectra, and then to combine all of these one-dimensional spectra into a single object spectrum. There are a number of issues to consider when combining spectra. First, the spectra may have come from different fibres, with differing throughputs, so that spectra need to be weighted properly before combination. Next, the data have slightly different velocity zero-points, necessitating conversion into the heliocentric frame before combination. Finally, the proper combination procedure must be used to suppress cosmic rays and other noise, while discarding as little data as possible.

The detailed procedure for combining spectra within IRAF is as follows. The full multifibre spectra were placed into the heliocentric frame using DOPCOR and then were split into one-dimensional spectra extending from 8470 to 8570 Å using the task SCOPY, thereby excising the contaminated red-most line of the Ca triplet. These one-dimensional spectra were rescaled by the corresponding fibre throughput, to make their flux values reflect the measured flux, rather than the throughput-corrected flux that is the default for WYFFRED.

Next, the spectra were combined using the SCOMBINE task. For combining, each spectrum was rescaled by its median flux, and then these rescaled spectra were combined using the median. Median combining was used only after considerable experimentation. For a Gaussian data set, the

median provides a  $\sim 20$  per cent noisier estimate of the true mean than the empirical mean of the data set. Thus, using the median rather than the mean effectively discards one third of the exposure time. However, this defect is outweighed by the superior non-Gaussian noise suppression of the median. In particular, the median strongly suppresses the residual cosmic rays left over from the earlier data processing steps. Once the data were combined, the continuum spectrum was subtracted. As the wavelength range was only 100 Å long by this point, the continuum was well represented by a third degree polynomial. Finally, the combined spectra were rebinned to the same 0.01 Å bin width.

As has been mentioned, the use of standard WYFFRED background subtraction did not suffice to remove the sky lines to within the accuracy of Poisson statistics. To circumvent this problem, we used the sky spectrum itself as a sky line detection filter. We convolved a sky spectrum with each combined spectrum, computed the integrated square of the convolution function, and then subtracted the amount of sky that would minimise this integral. In other words, residual sky lines were removed by adding or subtracting sky from the combined spectra until the convolution of the sky with the spectra was as small as possible. For most images, this made little difference, but for some, it noticeably reduced residual sky lines. The closest sky line was  $\sim 100$  km s<sup>-1</sup> removed from the mean velocity of Draco, so this procedure did not introduce systematic changes in measured stellar velocities. It did, however, reduce the incidence of double peaks and other artefacts in the final convolutions used to obtain stellar velocities.

### 3.3 Cross Correlation

To compute the velocity of stars from their spectra, we used the IRAF FXCOR package to cross-correlate each stellar

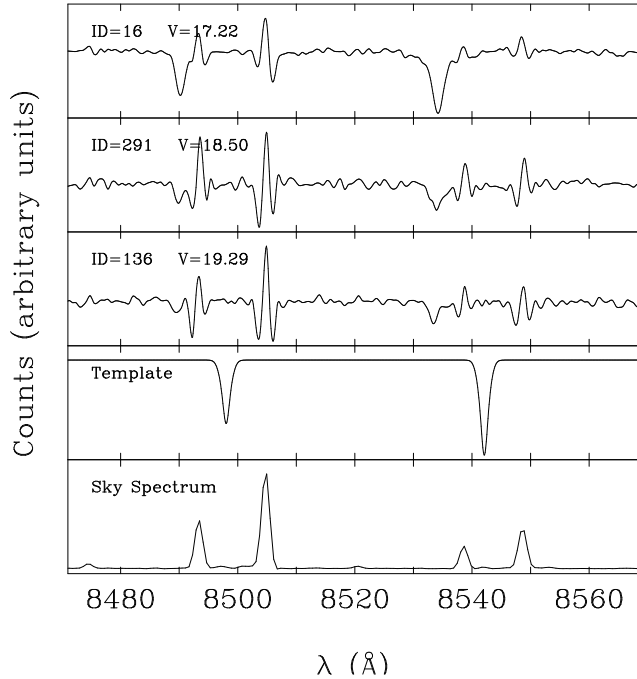


**Figure 2.** Top three panels: representative spectra of Draco member stars at three increasingly faint magnitudes. Fourth panel from top: the synthetic template used for the cross correlation, containing the two bluest lines of the Ca triplet. Bottom panel: typical sky spectrum showing the strong sky lines.

spectrum with a synthetic template spectrum composed of the two blue-most lines of the Ca triplet. In an approximate match of the stellar Ca lines, the template line at 8542 Å had a 50 per cent larger amplitude than the line at 8498 Å, and both lines were Gaussian with a full width half maximum of 2 Å.

The cross correlation was performed over the entire 8470 - 8570 Å range of the rebinned spectra. The peak of the cross-correlation function (CCF) was fit with a parabola spanning 20 rebinned pixels, or 2.0 Å. The details of the CCF fit had little influence on the final velocity, but they did affect the Tonry & Davis  $R_{TD}$  value errors reported by FXCOR. However, the velocity errors reported by FXCOR were subsequently recalibrated by a multiplicative constant so the latter effect was removed at the end. The 159 stars for which the CCF had a reasonably symmetrical unimodal peak were accepted as valid members, with accurate velocities. There were also 27 probable member stars with a poor quality CCF. These stars were excluded from our dynamics analyses because we did not judge their velocities to be reliable without additional corroborating observations.

Figure 2 shows the spectral region of interest for three representative spectra, after continuum subtraction. Additionally, the bottom panels of Figure 2 show the template spectrum and a typical sky spectrum. The presence of the blue-shifted Ca lines is clearly apparent in all of the spectra, including the faintest spectrum at  $V = 19.29$ . This figure also shows the proximity of the sky lines (bottom panel) to the shifted Ca lines, and the residuals of the sky lines in the final spectra.

### 3.4 Error Analysis

Accurate error estimation is perhaps the most difficult component of the data analysis. Unlike previous authors (Olszewski et al. 1996), we have only one epoch of data, preventing us from directly measuring the velocity uncertainties through  $\chi^2$  discrepancies of measurements taken at different times.

We employed two approaches to estimating the velocity errors. First, we recombined the brighter objects ( $V < 18.5$ ) into two final ‘split’ spectra, one composed of the odd numbered exposures and the other of the even exposures. We then cross-correlated these two spectra with the template separately and used the discrepancy between the two velocities obtained to estimate the true error  $\sigma_{\text{obs}}$  of the measurement (Figure 3, top panel). This error in turn was used to obtain a rescaling factor to apply to the Tonry & Davis  $R_{TD}$  value errors reported by FXCOR (Figure 3, centre panel). We found that we needed to rescale the FXCOR errors by 0.35 (Figure 3, centre panel, dotted line) to produce the desired  $\chi^2$  per degree of freedom of 1.0. From the centre panel of Figure 3, it is apparent that, after rescaling  $\sigma_{\text{obs}}$  by 0.35, only one  $3\sigma$  outlier remains, consistent with a well-behaved Gaussian error distribution with no extreme outliers.

Our second approach for estimating velocity errors was to build a Monte Carlo library of simulated observations, parameterised by stellar magnitude and effective (fibre throughput adjusted) exposure time. We then created an interpolation table of velocity error as a function of exposure time and magnitude. Next, we compared the discrepancies observed between the split spectra with those predicted by the interpolation table and found them to agree to within 10 per cent on average. However, the  $\sigma_{\text{obs}}$  of a small num-

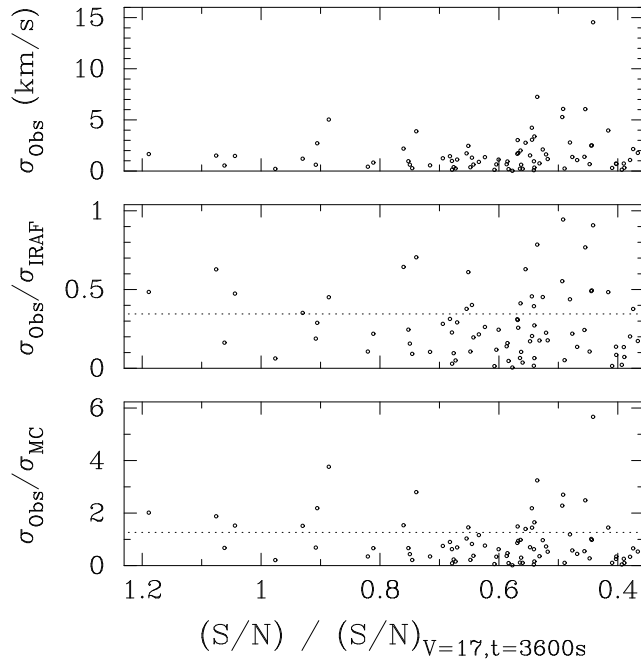


**Figure 3.** Top panel: empirical velocity errors as a function of  $S/N$  relative to the  $S/N$  of a  $V = 17$  star observed for one hour. These errors were obtained by dividing the spectra of bright stars into two batches, using these batches to obtain two velocities, and dividing the difference between the two velocities by  $\sqrt{2}$  to give the velocity error at each point. Centre panel: ratio of the above empirical errors to the nominal IRAF velocity uncertainty. The dotted line at 0.35 is the number by which the IRAF errors must be rescaled to give the expected  $\chi^2$  per degree of freedom. Bottom panel: errors predicted by Monte Carlo simulations, and the rescaling (dotted line) necessary to make these errors agree with the empirical errors of the top panel. As the Monte Carlo errors produce 4 to  $5\sigma$  outliers when used to predict the observed errors, so we elected to use the well-behaved rescaled IRAF errors of the centre panel as the basis of our error model.

ber of the split spectra disagreed by 4 to  $5\sigma$  with the value predicted by the table (Figure 3, bottom panel, outliers).

On the basis of this error analysis, we elected to reject the Monte Carlo approach, and model our errors by rescaling the FXCOR errors by 0.35. This rescaling was used for the entire data set including those stars too faint to be split into two usable spectra. Of the 284 stars for which we obtained velocities, 203 had good quality velocities as judged by a clear peak in the CCF. Of these 203 stars, 159 were Draco members. An additional 27 stars were probable members, but the CCF was multi-modal or highly asymmetric. Figure 4 shows a histogram of stellar velocities of the stars with valid velocities, extending to the velocity of the first star judged to be a non-member. The separation between Draco members and Galactic contaminant stars is very clear, and there is little likelihood of non-Draco stars being included in the sample.

It is apparent that many of the stars have a low Tonry & Davis (1979)  $R_{TD}$  value; 10 stars of the 159 star sample have  $R_{TD} < 2$ . Tonry & Davis (1979) point out that the velocity error formula  $\sigma_v \propto (1 + R_{TD})^{-1}$  begins to break down for small values of  $R_{TD}$ , and attribute this breakdown to the selection of false CCF peaks. This may be worrisome, because our IRAF-based velocity errors depend on the validity of this error scaling. However, this problem is mitigated in several ways. First, we reject stars with an obviously multi-modal CCF. Next, our Monte-Carlo simulations indicate that reliable velocities are possible even for the faint stars of our sample, demonstrating that wildly spurious CCF peaks oc-

cur infrequently. Finally, we note that the effect of additional velocity errors is milder than the effect of additional binaries, which we model extensively. For instance, in our following dynamical analyses, we assume binary distributions that have between 5 and 15 binaries moving faster than  $10 \text{ km s}^{-1}$ , and demonstrate that these have little effect on our dynamical inferences. Nevertheless, in the following sections, we repeat some of our analyses using subsamples of stars with  $R_{TD} > 5$  and  $R_{TD} > 7$  to demonstrate that our dynamics conclusions remain unchanged if we limit our analysis to high quality spectra.

### 3.5 Velocity Results

The mean velocity of the 159 star sample, including the heliocentric correction but before a zero-point velocity correction, is  $-290.6 \pm 0.8 \text{ km s}^{-1}$ . This agrees with the values  $-293.3 \pm 1.0 \text{ km s}^{-1}$  measured by AOP, and  $-293.8 \pm 2.7$  measured by Hargreaves et.al. (1996) at the  $2.1\sigma$  level. However, our zero point correction obtained from the twilight sky frames produces a corrected mean velocity equal to  $-287.1 \pm 0.9 \text{ km s}^{-1}$ , which is not in agreement with these previous data. The source of this  $4.6\sigma$  discrepancy is unknown.

In lieu of using our questionable velocity zero point, we instead elect to use the 61 stars common to our data set and that of AOP to calibrate the mean velocity our data. The mean (median) velocity difference between the two data sets is  $-1.22$  ( $1.36$ )  $\text{km s}^{-1}$ ; accordingly, our reported velocities

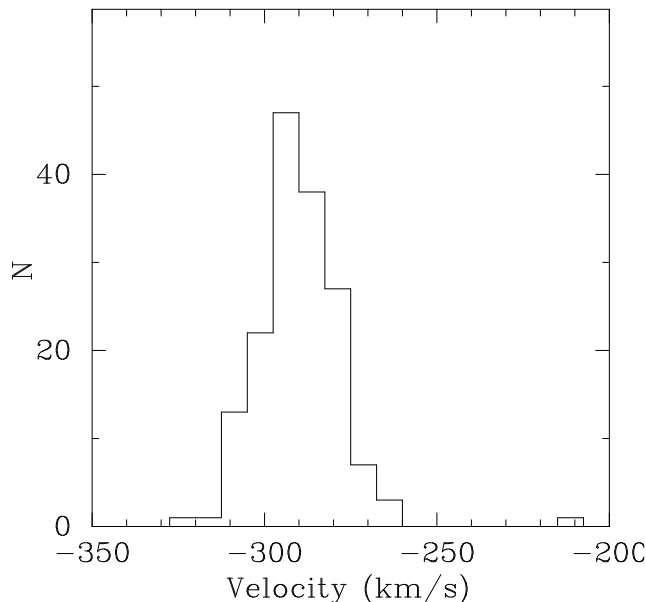


**Figure 4.** Histogram of stellar velocities of observed stars, including the closest member of Galactic contaminant population at  $\sim 220$   $\text{km s}^{-1}$ .

are adjusted by a zero point correction of  $+1.22$   $\text{km s}^{-1}$ . This adjustment leaves the mean velocity of our entire data set, including stars not present in previous data, in  $1.1\sigma$  agreement with the entire AOP data set.

The twilight sky images, although apparently unsuitable for a precise zero point calibration, did demonstrate that we maintained stable relative velocities throughout the observing run. The RMS scatter of the nightly mean velocity of the solar Ca lines was  $0.34$   $\text{km s}^{-1}$  across the four observing nights.

Table 1 gives the 159 member stars with good velocities. The first column is our internal target identification number. For stars with velocities also measured by AOP, the second column gives their primary name for this star. The other columns provide J2000 right ascension and declination, velocity, velocity uncertainty, and Tonry & Davis (1979)  $R_{\text{TD}}$  value of the CCF. The velocity has been adjusted by  $+1.22$   $\text{km s}^{-1}$  to match the mean velocity of AOP. Table 2 gives the remaining 27 probable member stars. These stars have a multi-modal or strongly asymmetric CCF, and were not included in our subsequent dynamics analyses. The one star ( $ID=273$ ) of these 27 that also appears in the previously published data set of AOP is in  $2.9\sigma$  disagreement with this previous published velocity, supporting our decision to reject it based on its CCF.

## 4 BINARIES

In this section, we first discuss the importance of corrections for binaries and then compare the velocities of stars in our dataset with the previous data set of AOP. We use the disagreement between the two to constrain the number of radial velocity variables and hence Draco’s binary fraction.

### 4.1 The Effects of Binaries

When analysing kinematical data, it is important to take into account the effect of binary stars on the velocity distribution. Binaries tend to inflate the apparent velocity distribution. Equally important, the presence of a binary-induced tail increases the uncertainty of the measured velocity dispersion, an effect that needs to be taken into account carefully when reporting the kinematical properties of dSphs. Past work has shown that binary stars probably do not explain the gross velocity dispersions of the dSphs. Olszewski, Pryor & Arnandorff (1996) used Monte Carlo simulations to demonstrate that binary stars have a negligible effect on the velocity dispersion and the inferred mass-to-light ratio of both Ursa Minor and Draco. However, they also concluded that, in the decade of binary period around one year, binary stars may be 3 to 5 times more abundant in these two dSphs than in the solar neighbourhood. Hargreaves, Gilmore & Annan (1996) used similar modeling to show that binary stars could affect the observed velocity distribution only if the distribution of orbital parameters were significantly different from that of solar neighbourhood binaries.

Nevertheless, these findings are not completely general. Although binaries may not affect the velocity dispersion significantly, they may nevertheless have an influence on more sophisticated forms of dynamical model fitting. The presence of binaries may give a distribution that is qualitatively different from a binary-free distribution: for example, binaries could produce a velocity tail that is incompatible with a truncated distribution like a King model. Empirically, we note the inclusion of binaries into a maximum likelihood analysis of the velocity dispersion usually does not significantly shift the most likely dispersion of a dataset; it does, however, tend to expand the error bars, so that omitting binaries may lead one to overestimate the statistical significance of observed spatial variations of the dispersion. For

**Table 1** Observed member stars -  $ID$  is the identification number in our target catalogue;  $ID_{AOP}$  is the designation of the object in the previous data set of Armandroff, Olszewski, & Pryor (1995);  $V$  is the  $V$ -band magnitude;  $RA$  and  $Dec$  are the J2000 coordinates;  $v$  and  $\sigma_v$  are measured heliocentric velocity and its uncertainty; and  $R_{TD}$  is the Tonry & Davis (1979)  $R$  value of the cross-correlation function.

$ID$	$ID_{AOP}$	$V$	$RA$	$Dec$	$v$	$\sigma_v$	$R_{TD}$	$ID$	$ID_{AOP}$	$V$	$RA$	$Dec$	$v$	$\sigma_v$	$R_{TD}$
14		18.26	17 19 16.94	+58 15 50.8	-290.17	1.81	5.2	154	G	17.69	17 20 27.42	+57 56 52.4	-291.41	0.80	13.0
16	13784	17.22	17 21 02.26	+58 15 38.3	-277.35	0.89	12.2	158		19.20	17 20 11.09	+57 56 45.7	-278.82	2.27	3.7
23		18.43	17 20 14.55	+58 12 51.4	-301.23	2.11	4.2	160	273	18.37	17 19 50.11	+57 56 40.7	-281.15	2.46	3.7
29		18.49	17 18 05.77	+58 11 22.0	-286.57	1.91	4.3	163		18.43	17 22 11.25	+57 56 33.2	-311.32	1.92	4.6
39		19.35	17 18 45.87	+58 07 32.7	-265.70	4.57	1.8	166	473	17.61	17 19 36.06	+57 56 29.0	-288.50	0.68	16.9
43		18.41	17 19 53.89	+58 06 44.1	-277.69	1.47	7.0	168		19.01	17 20 14.84	+57 56 25.6	-286.26	3.36	2.3
47		18.24	17 17 58.39	+58 05 58.6	-297.89	3.37	2.4	171		18.61	17 21 17.93	+57 56 21.4	-291.42	1.76	5.4
48		19.49	17 20 32.16	+58 05 39.9	-280.82	3.57	1.9	173		18.66	17 20 40.35	+57 56 18.2	-292.09	1.46	6.9
49		18.87	17 20 23.76	+58 05 24.2	-309.12	2.50	3.4	174		18.40	17 19 53.52	+57 56 16.5	-295.86	1.38	7.5
50		19.12	17 19 37.13	+58 05 20.1	-274.43	2.59	3.7	176	L	18.32	17 20 17.07	+57 56 12.3	-295.03	1.14	9.4
52		19.13	17 21 05.85	+58 04 55.0	-290.10	3.88	1.6	177		19.52	17 22 06.60	+57 56 10.4	-302.82	4.23	2.0
55		17.32	17 17 38.58	+58 04 38.4	-267.13	0.81	12.4	184	3309	18.37	17 21 03.26	+57 55 59.4	-290.53	0.84	13.2
57	XI-13	17.23	17 18 52.15	+58 04 13.0	-295.45	0.75	15.8	185		18.18	17 17 55.41	+57 55 59.0	-291.46	1.27	7.8
62	XI-7	17.44	17 19 12.30	+58 02 57.8	-291.15	1.11	10.0	186		18.95	17 19 26.83	+57 55 51.8	-279.99	1.77	5.0
63		18.91	17 19 36.67	+58 02 50.4	-290.18	2.44	3.6	187		19.18	17 21 41.83	+57 55 50.9	-283.17	2.86	2.7
66		19.25	17 20 56.62	+58 02 35.2	-283.19	2.53	3.5	189	20083	17.83	17 18 57.81	+57 55 46.3	-296.67	1.22	8.4
68		19.17	17 21 22.32	+58 02 15.7	-307.75	2.30	4.4	192	3116	18.57	17 19 22.97	+57 55 30.8	-280.06	1.68	5.7
69	17557	18.24	17 21 04.89	+58 02 01.2	-298.34	1.34	7.7	197		19.06	17 20 24.16	+57 55 15.6	-289.69	2.10	4.2
70		18.34	17 19 21.85	+58 01 52.3	-295.77	1.22	8.5	198	286	17.81	17 19 45.19	+57 55 14.4	-297.05	0.89	12.8
71	17871	17.26	17 18 08.10	+58 01 46.7	-310.44	0.50	21.8	199		19.84	17 18 24.05	+57 55 08.1	-303.03	5.46	1.4
74		19.02	17 20 01.59	+58 01 33.7	-295.27	1.21	8.4	201		18.36	17 19 57.37	+57 55 04.8	-306.26	1.88	5.5
76		19.77	17 22 02.34	+58 01 17.4	-296.01	5.35	1.4	205		19.10	17 20 44.74	+57 54 59.9	-293.71	3.94	2.2
79		18.78	17 20 18.03	+58 01 12.1	-287.73	2.68	3.5	206		19.25	17 21 35.42	+57 54 59.5	-296.36	2.90	2.4
83		19.08	17 21 37.81	+58 00 52.5	-282.70	3.37	2.5	208	297	17.85	17 19 41.21	+57 54 56.8	-285.52	0.82	14.0
84		18.79	17 18 35.67	+58 00 50.1	-289.61	3.30	2.4	212		18.73	17 20 25.02	+57 54 50.8	-277.27	1.40	6.4
85		18.40	17 19 21.76	+58 00 40.6	-275.48	1.49	7.0	216	3297	17.89	17 20 53.79	+57 54 40.8	-284.47	1.09	9.8
86		18.85	17 20 15.27	+58 00 35.1	-296.57	1.61	6.5	219		18.31	17 18 44.56	+57 54 38.3	-284.47	1.24	8.9
92		19.09	17 19 07.79	+58 00 19.8	-287.45	3.26	3.0	220		18.96	17 19 10.33	+57 54 37.7	-295.81	2.44	3.4
93		19.13	17 22 06.12	+58 00 12.0	-289.21	3.19	2.3	222		18.34	17 19 57.73	+57 54 35.3	-296.41	1.04	10.4
96	581	17.73	17 20 34.81	+57 59 56.9	-297.70	0.70	17.0	223		18.83	17 20 07.52	+57 54 32.8	-299.08	1.89	4.8
98	3363	17.39	17 20 47.82	+57 59 55.6	-294.30	0.91	12.7	224		18.09	17 19 17.65	+57 54 32.4	-289.52	1.36	7.7
99		18.37	17 18 41.42	+57 59 52.1	-262.99	1.85	5.7	230	490	17.66	17 19 40.04	+57 54 24.9	-304.72	0.74	15.2
100	3361	17.58	17 20 52.10	+57 59 47.8	-294.43	0.90	12.5	233	IX-18	17.77	17 18 57.66	+57 54 14.3	-278.58	1.14	8.8
101		18.40	17 19 20.05	+57 59 43.1	-306.59	2.13	4.3	240	IV-18	17.47	17 22 10.75	+57 53 57.4	-324.43	0.63	16.2
104	18281	18.11	17 21 56.99	+57 59 33.9	-314.16	5.37	1.6	245	K	18.23	17 19 55.86	+57 53 48.8	-293.61	1.43	7.3
105	449	17.51	17 19 51.86	+57 59 17.9	-302.99	0.76	15.2	248	H	18.28	17 20 15.77	+57 53 43.5	-298.30	1.30	8.2
106	X-11	17.18	17 19 10.88	+57 59 17.2	-297.17	0.72	15.4	250		18.65	17 21 49.22	+57 53 37.2	-291.54	2.04	4.7
107		18.54	17 19 56.45	+57 59 16.1	-294.55	3.06	2.9	253	361	17.56	17 20 34.22	+57 53 32.1	-286.16	0.94	12.5
109	18723	17.20	17 18 42.30	+57 59 10.0	-290.49	0.77	14.2	259		18.00	17 20 17.01	+57 53 12.4	-290.06	1.14	10.2
111	437	17.69	17 20 17.06	+57 59 02.1	-304.97	1.37	7.5	262	IV-20	17.39	17 22 13.68	+57 53 06.7	-300.23	0.77	14.6
112		18.40	17 17 38.60	+57 58 54.1	-285.65	3.42	2.5	265		18.68	17 19 57.10	+57 52 58.1	-272.54	1.68	5.7
115	3053	17.46	17 19 35.51	+57 58 46.6	-282.60	1.04	11.3	270		19.04	17 21 13.88	+57 52 46.0	-280.86	3.38	2.7
116	461	17.26	17 19 42.44	+57 58 37.7	-293.36	3.07	2.4	272		18.48	17 19 56.66	+57 52 43.0	-295.53	1.38	8.3
117		19.07	17 21 36.85	+57 58 37.1	-303.84	2.97	2.3	275	IX-5	17.53	17 19 13.51	+57 52 33.6	-286.74	0.99	11.4
121		18.78	17 20 41.10	+57 58 25.7	-295.70	2.20	3.8	278		18.54	17 19 56.98	+57 52 23.1	-272.94	1.93	5.1
122		18.48	17 20 34.12	+57 58 22.7	-296.04	1.81	5.4	279		18.29	17 21 14.27	+57 52 22.5	-290.85	1.34	7.9
123		18.46	17 20 10.54	+57 58 20.9	-272.80	1.25	8.1	284	21456	17.15	17 18 10.43	+57 52 09.2	-306.42	0.55	19.3
125	3339	18.11	17 20 53.77	+57 58 12.6	-288.64	1.36	8.2	285	343	17.63	17 20 13.59	+57 51 59.4	-294.22	1.11	10.1
129		19.32	17 20 33.53	+57 58 06.2	-286.38	3.40	1.8	286	350	18.35	17 20 20.44	+57 51 58.4	-292.34	1.10	9.8
130	427	18.14	17 20 31.22	+57 58 05.5	-302.57	1.33	7.7	287		18.65	17 20 56.73	+57 51 57.5	-292.73	2.43	3.9
134	11	17.64	17 20 05.74	+57 57 52.7	-284.28	0.82	13.9	288		19.13	17 19 13.94	+57 51 55.2	-298.03	2.31	3.4
136		19.29	17 18 25.19	+57 57 45.6	-302.00	2.66	2.7	291		18.50	17 18 30.61	+57 51 47.0	-283.07	2.46	3.9
138		18.90	17 22 43.71	+57 57 30.8	-279.77	1.76	5.8	295	506	18.04	17 19 53.13	+57 51 38.0	-303.70	1.06	8.8
141		19.06	17 22 18.65	+57 57 19.4	-281.89	2.49	3.5	297		18.82	17 20 02.03	+57 51 30.5	-312.78	1.71	5.6
145	3316	17.40	17 21 03.60	+57 57 08.3	-287.75	0.69	16.2	299	3150	17.38	17 19 36.37	+57 51 25.1	-280.42	0.77	14.5
146		18.60	17 20 24.57	+57 57 08.2	-290.76	1.51	6.6	301	3255	18.26	17 20 39.90	+57 51 15.4	-282.95	1.31	8.1
149	22	18.22	17 20 01.66	+57 57 04.6	-296.58	1.18	8.9	302	3267	17.92	17 20 51.00	+57 51 09.8	-282.19	1.02	8.9
151	45	17.76	17 19 57.99	+57 56 58.4	-292.71	1.11	10.1	306		19.41	17 19 23.31	+57 51 01.4	-289.71	3.04	2.6

**Table 1, continued** Observed member stars

<i>ID</i>	<i>ID</i> <sub>AOP</sub>	<i>V</i>	<i>RA</i>	<i>Dec</i>	<i>v</i>	$\sigma_v$	<i>R</i> <sub>TD</sub>	<i>ID</i>	<i>ID</i> <sub>AOP</sub>	<i>V</i>	<i>RA</i>	<i>Dec</i>	<i>v</i>	$\sigma_v$	<i>R</i> <sub>TD</sub>
308		18.26	17 19 49.43	+57 51 00.7	-276.42	0.89	11.3	343		18.80	17 20 59.36	+57 47 22.1	-301.45	1.84	4.8
309	21845	18.04	17 18 32.90	+57 50 56.4	-289.93	1.25	8.4	344		18.78	17 20 34.57	+57 47 17.9	-272.26	3.17	2.6
310		18.30	17 20 31.72	+57 50 55.2	-285.32	1.07	10.3	346	VI-5	17.88	17 20 40.25	+57 47 07.2	-299.63	2.37	3.9
311	522	18.18	17 20 13.45	+57 50 51.8	-283.24	0.92	12.2	350	VIII-25	17.94	17 19 03.66	+57 46 42.7	-282.53	1.88	5.3
312		18.71	17 20 39.77	+57 50 50.2	-301.66	3.50	2.2	351	V-27	18.02	17 21 39.42	+57 46 40.4	-310.59	1.32	7.7
315	3237	17.58	17 20 33.59	+57 50 19.7	-277.00	2.20	3.6	352		18.86	17 21 00.24	+57 46 38.0	-303.39	1.73	5.5
316	3210	18.11	17 20 05.43	+57 50 18.3	-288.99	1.33	7.6	354	VII-8	17.81	17 20 09.82	+57 46 29.7	-293.85	0.82	13.4
317	IV-14	17.56	17 21 30.33	+57 50 16.4	-304.75	1.07	9.5	356		18.44	17 19 34.43	+57 46 11.9	-286.53	1.45	6.2
318		18.89	17 19 22.60	+57 50 13.1	-300.34	2.20	4.6	357		18.98	17 20 18.66	+57 46 01.5	-304.12	1.62	6.0
319		18.82	17 19 32.88	+57 49 49.0	-289.04	3.27	2.4	358		19.01	17 22 27.17	+57 45 54.7	-294.71	2.07	4.3
320	3213	18.17	17 20 11.71	+57 49 36.5	-294.10	1.36	7.8	362		18.90	17 22 03.68	+57 45 07.5	-287.88	1.85	5.3
324	22209	17.63	17 20 21.19	+57 49 27.3	-294.40	0.77	14.8	363		18.82	17 20 55.60	+57 44 34.7	-304.18	2.75	2.7
325		19.34	17 19 37.77	+57 49 18.7	-292.68	5.12	1.5	365		19.15	17 18 56.16	+57 43 45.7	-281.69	3.71	1.8
328		18.64	17 19 20.05	+57 49 04.9	-295.53	1.30	8.3	368		18.41	17 18 13.07	+57 42 46.8	-286.95	2.34	3.4
329		18.52	17 20 45.48	+57 49 00.3	-282.97	1.12	10.0	371		18.03	17 17 46.21	+57 42 22.0	-299.06	0.93	10.6
330	VIII-17	17.58	17 18 58.35	+57 48 57.7	-300.03	0.68	16.4	375		17.68	17 22 03.80	+57 41 28.9	-294.16	2.26	4.0
331		19.36	17 20 02.86	+57 48 57.3	-284.27	2.65	3.1	378		19.88	17 21 03.78	+57 39 54.6	-284.27	3.38	2.4
334	VII-4	17.24	17 19 47.77	+57 48 36.7	-280.52	0.82	14.0	383		17.93	17 18 43.05	+57 38 50.1	-296.48	0.76	14.2
337		18.62	17 19 34.74	+57 48 05.3	-294.50	2.40	3.8	385		18.71	17 20 51.24	+57 38 14.6	-306.37	1.99	5.0
338		19.14	17 22 33.56	+57 48 04.0	-275.44	3.12	2.7	386		18.26	17 21 10.23	+57 38 02.7	-307.98	2.59	3.3
339	22626	18.41	17 21 10.47	+57 47 53.5	-307.50	1.40	7.4	400		17.99	17 19 31.97	+57 33 35.3	-309.02	1.78	4.3
342	V-26	17.41	17 21 40.41	+57 47 32.3	-293.20	0.79	13.8								

**Table 2** Probable Member stars - stars with velocities that indicate probable Draco membership, but with a multi-modal or highly asymmetric cross-correlation function. Columns are the same as in Table 1.

<i>ID</i>	<i>ID</i> <sub>AOP</sub>	<i>V</i>	<i>RA</i>	<i>Dec</i>	<i>v</i>	$\sigma_v$	<i>R</i> <sub>TD</sub>	<i>ID</i>	<i>ID</i> <sub>AOP</sub>	<i>V</i>	<i>RA</i>	<i>Dec</i>	<i>v</i>	$\sigma_v$	<i>R</i> <sub>TD</sub>
3		18.78	17 20 36.06	+58 23 40.8	-292.36	7.86	1.6	273	335	18.18	17 20 06.97	+57 52 37.3	-274.88	3.88	2.0
13		18.85	17 18 06.88	+58 15 55.5	-289.49	4.75	1.1	276		19.10	17 18 31.14	+57 52 28.1	-302.25	4.23	2.2
18		18.69	17 21 42.56	+58 14 33.1	-276.97	4.35	2.4	277		19.56	17 20 45.61	+57 52 24.8	-302.09	5.58	0.8
30		19.39	17 20 24.22	+58 11 20.5	-328.94	4.82	1.6	281		19.51	17 20 13.23	+57 52 19.8	-291.10	4.74	1.4
64		19.09	17 20 06.08	+58 02 50.3	-277.76	4.05	1.5	293		18.89	17 20 44.60	+57 51 39.7	-288.47	3.49	2.3
75		18.88	17 19 57.95	+58 01 20.1	-307.67	3.89	1.6	304		19.74	17 21 22.25	+57 51 03.9	-284.71	4.53	0.8
80		19.62	17 21 07.79	+58 01 09.5	-313.54	4.07	0.8	305		18.96	17 19 18.69	+57 51 03.7	-293.41	4.19	1.9
140		19.69	17 20 55.57	+57 57 20.5	-269.48	8.27	1.4	333		19.44	17 20 16.57	+57 48 40.5	-288.42	3.89	1.7
153		19.64	17 21 38.81	+57 56 57.3	-285.46	4.48	1.2	336		19.67	17 20 59.09	+57 48 16.2	-290.32	4.08	1.6
164		19.27	17 18 45.70	+57 56 29.3	-287.29	3.45	2.1	345		19.14	17 19 04.39	+57 47 08.9	-294.31	3.24	2.2
203		19.64	17 20 15.90	+57 55 02.9	-303.53	5.17	1.1	374		19.45	17 18 50.95	+57 41 37.7	-288.88	4.98	1.2
236		19.21	17 17 56.52	+57 54 00.7	-287.88	3.09	2.4	376		19.50	17 17 33.69	+57 41 02.1	-296.79	3.34	1.8
254		19.64	17 19 56.29	+57 53 29.7	-296.04	4.48	1.1	401		19.66	17 19 55.18	+57 33 00.7	-272.36	4.30	1.1
255		19.02	17 20 41.62	+57 53 16.8	-285.73	3.64	1.9								

these reasons, we include plausible binary distributions into our analyses.

For the purpose of this work, we draw velocity measurements from the Duquennoy & Mayor (1991, hereafter DM) binary data set. This is a set of binary orbital elements drawn from a sample of 165 solar-type primary stars in the solar neighbourhood. Of the stars in the DM sample, 71, or 41 per cent, have companions. Fifty-two of these 71 multiples have known binary orbital elements. The distribution of the period  $P$  is fit by a log-normal profile, the eccentricity  $e$  is fit by Gaussian ( $P < 10$  days) or boxcar ( $P > 10$  days) distributions, and the mass ratio  $q$  is fit by a truncated Gaussian. Using the DM orbital element distribution, we construct a cumulative distribution of binary radial velocities and use this to build an interpolation table of the differential binary radial velocity distribution. We then convolve the differential distribution with model radial profiles

to obtain the observed model profile.

Additionally, we also construct a modified DM distribution with which we simulate giant branch binary evolution. We draw binaries from the empirical DM distribution, discard those binaries with a periastron  $< 30R_{\odot}$ , circularise the orbit by setting  $e = 0$  and making the new circular radius equal to the original semilatus rectum, and, finally, reduce the angular momentum by 20 per cent. This picture of binary evolution is justified by noting that the semilatus rectum is a function of angular momentum, which is largely preserved during the circularisation phase. The 20 per cent magnitude of the subsequent angular momentum change is at the upper range of the 10 to 20 per cent range observed in simulations (Hurley, Tout, & Pols 2001). Figure 5 shows the cumulative probability distribution of radial velocities drawn from the unevolved and evolved DM distributions. It is evident that binary evolution significantly increases the

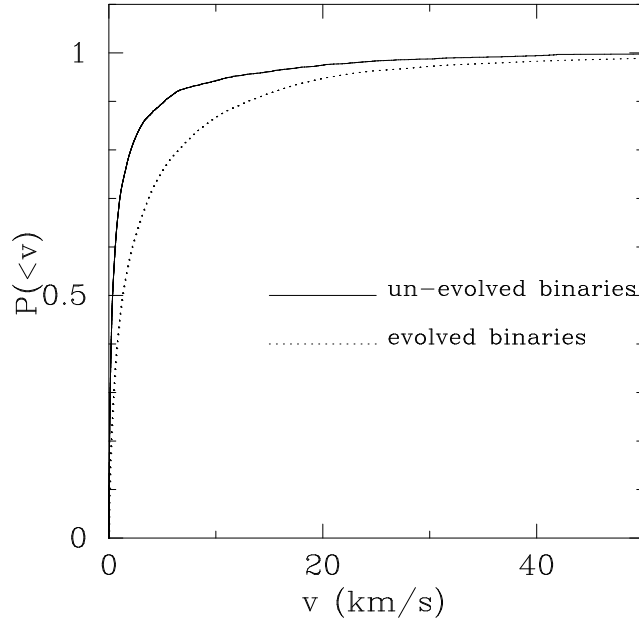


**Figure 5.** Cumulative probability distribution of the absolute value of the radial velocities of binaries drawn from two models. The solid (unevolved) model is taken from the Duquennoy & Mayor (1991) solar neighbourhood binary distribution; the dashed (evolved) model is obtained by circularising the orbits of the unevolved model, and then reducing angular momentum by 20 per cent, in a crude approximation of tidal dragging caused by giant branch evolution.

number of fast, short period binaries. For instance, evolution doubles the number of binary stars observed, at any moment, with a velocity  $> 10 \text{ km s}^{-1}$ . Most of the difference between the evolved and un-evolved distributions arises during orbit circularisation, and substituting a 10 per cent angular momentum loss for the 20 per cent used has little effect on the resulting binary velocity distribution.

#### 4.2 Draco's Binary Fraction

Evidence on the binary fraction can be gleaned on comparison of our dataset to previously obtained velocities in Draco. The largest set of Draco observations overlapping with our dataset is the 91 velocities obtained by AOP. The 19 star data set of Hargreaves et al. (1996) also covers the central region of Draco, but is redundant for the purpose of our comparison, given its good agreement with the larger dataset of AOP. Furthermore, AOP claim that Hargreaves et al. (1995) underestimate their velocity errors, so that any calibration of our dataset with that of Hargreaves et al. (1995) would not be independent of the dataset of AOP.

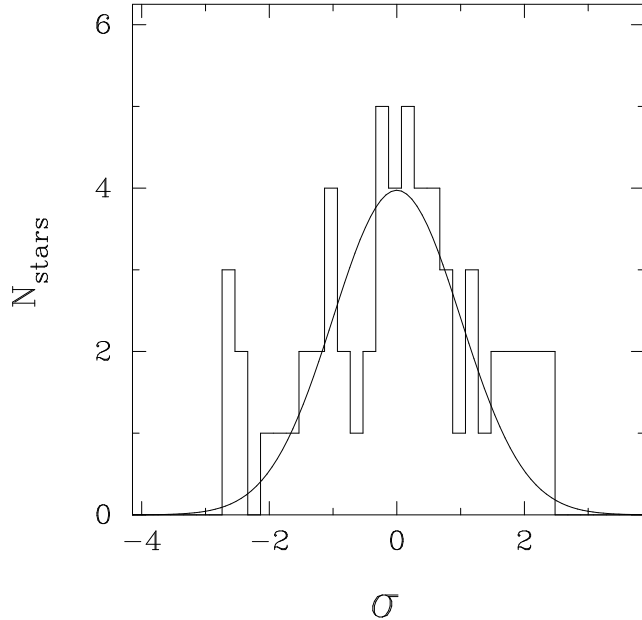
The data of AOP were obtained with the KPNO 4m telescope and the HYDRA multifibre spectrograph. These data were obtained over a period of nearly two years and covered a spectral range was 4720 to 5460 Å containing H $\beta$  and the Mg triplet. Velocity uncertainties were computed both by using simulated data to rescale FXCOR errors, and by measuring the scatter of measurements at multiple epochs. Hence, the velocity uncertainty estimates of these data are on a firm footing and can be used to probe the validity of our own errors. Although we made no special attempt to re-observe the stars of AOP, 61 of our 159 quality Draco members are also present in the previous dataset.

Figure 6 depicts a histogram of the disagreement be-

tween the two datasets in units of Gaussian  $\sigma$ , after subtracting a  $1.22 \text{ km s}^{-1}$  mean offset. Although there are no  $3\sigma$  outliers, there is an apparent excess of points between 2 and  $3\sigma$ . This disagreement is reflected in the  $\chi^2$  per degree of freedom of  $\chi^2/N_{\text{DOF}} = 1.77$  with  $p(> \chi^2) = 0.00035$ .

However, this disparity is readily explained by the presence of binaries. We ran a simulation of the disagreement between our data set and that of AOP, contaminating both sets of data in parallel with binaries drawn from the distribution of DM. For this simulation, we assumed various binary fractions and a 5 year baseline between measurements. In the presence of binaries, we found that 32 per cent ( $1\sigma$ ) of the time,  $\chi^2/N_{\text{DOF}} > 2.4$  for unevolved binaries with a low 20 per cent binary fraction. For a more realistic 50 per cent binary fraction,  $\chi^2/N_{\text{DOF}} > 7.5$  32 per cent of the time. Similarly, an 80 per cent unevolved binary fraction is ruled out with 95 per cent certainty because the observed  $\chi^2$  disparity is too small. An evolved binary distribution, which has a greater number of rapid orbits arising from angular momentum loss, is even more strongly constrained: a 50 per cent evolved binary fraction is ruled out with 0.95 certainty, and an 80 per cent evolved fraction is ruled out at the 99.7 per cent ( $3\sigma$ ) level.

The data are completely consistent with a binary distribution and fraction comparable to those in the solar neighbourhood. Unless either we or AOP significantly overestimated our velocity uncertainties, creating a very low intrinsic  $\chi^2$  that would counteract the binary-induced component of  $\chi^2$ , then a very large binary fraction such as suggested by AOP is ruled out at the 2 to  $3\sigma$  level. Even if we repeat the simulations, assuming that we over-estimated our errors by factor of 2, we can still rule out an unevolved binary fraction exceeding 80 per cent and an evolved binary fraction exceeding 50 per cent at the 0.95 significance level.



**Figure 6.** Difference (in units of Gaussian  $\sigma$ ) between our measured Draco stellar velocities and the velocities of the same 61 stars measured previously by AOP. Although there is an excess of stars between 2 and 3 $\sigma$  and the  $\chi^2$  per degree of freedom is  $\chi^2/N_{\text{DOF}} = 1.77$ , this large  $\chi^2$  can be explained with binaries. Indeed, the absence of large outliers argues against the claim of a very large binary fraction made by AOP.

An immediate question that arises is why our analysis of essentially the same data gives a different result for the binary fraction than the original work of AOP. AOP regarded individual  $\chi^2$  outliers as binaries, effectively considering only binaries with velocities that disagreed between measurements at the  $p = 0.001$  ( $3.3\sigma$ ) level. From the presence of six apparent binaries in the combined Ursa Minor and Draco datasets, AOP extrapolated a binary fraction several times larger than that of the solar neighbourhood, with large uncertainties. However, these  $\chi^2$  outliers could have resulted from a mild misestimation of the velocity errors for these stars. Our upper limit on the binary fraction, however, is based on the absence of outliers and is sensitive to an over-estimation of velocity errors. For these reasons, we believe that our analysis is more likely to be robust against error misestimation or data corruption, and that there is no evidence supporting a large binary fraction.

## 5 OBSERVED KINEMATICS

### 5.1 Radial Variation of the Velocity Dispersion

Although nearly 100 velocities have been measured in Draco prior to this work, they have revealed little about the radial variation of the velocity dispersion. As previous spectroscopic targets were selected using relatively imprecise photographic plate photometry, Galactic foreground contamination limited velocity measurements to the dense centre of the dSph, where dSph member yield is high. Hargreaves et al. (1996) found that the velocity dispersion appears to be flat or to rise with radius, and is inconsistent with the best-fit King model profile at the  $2\sigma$  level; however their data had only three points outside the core radius. The data of this paper, in contrast, contain 33 points outside  $10'$  (approximately the King core radius), and include several stars

very close to the King tidal radius, where the velocity should drop to zero under the King model hypothesis.

When computing the velocity dispersion as a function of radius, we use a maximum likelihood technique which assumes that the velocity uncertainties are Gaussian and that the velocity distribution in any radial bin is a Gaussian centred on the mean velocity  $\bar{v}$  of the entire ensemble. Furthermore, we assume that the stars are drawn from a binary distribution with a radial velocity probability distribution  $P_b(v)$ . The observed velocity distribution is then the assumed Gaussian profile convolved with observational errors and  $P_b(v)$ .

The probability distribution of the true velocity dispersion  $\sigma_v$  of the bin is then given by

$$P(\langle v^2 \rangle) \propto \prod_i \int_{-\infty}^{+\infty} \frac{\exp\left(-\frac{1}{2} \frac{(v_i - v' - \bar{v})^2}{\sigma_i^2 + \langle v^2 \rangle}\right)}{\sqrt{2\pi(\sigma_i^2 + \langle v^2 \rangle)}} \times [(1-f)\delta(v') + f P_b(v')] dv' \quad (1)$$

where  $v_i$  and  $\sigma_i$  are the  $i^{\text{th}}$  velocity in the bin and its uncertainty,  $f$  is the binary fraction,  $\delta$  is the usual Dirac delta function, and  $\bar{v}$  is the mean velocity of the entire ensemble. In practice, we speed the computations by using Fourier convolutions to create a library of  $P(\langle v^2 \rangle)$  parameterised by  $\sigma^2 + \langle v^2 \rangle$ . Numerical integration of the tabulated  $P(\langle v^2 \rangle)$  then gives the uncertainties of the velocity dispersion.

Figure 7 shows a set of plots of velocity dispersions, assuming various binary fractions. As pointed out by Oh, Aarseth & Lin (1995), tidal disruption can have the appearance of rotation, because the first order expansion of the tidal field produces a stretching force that, in projection, causes motion similar in appearance to rotation. Therefore, in the bottom row of Figure 7, we also plot the velocity dis-

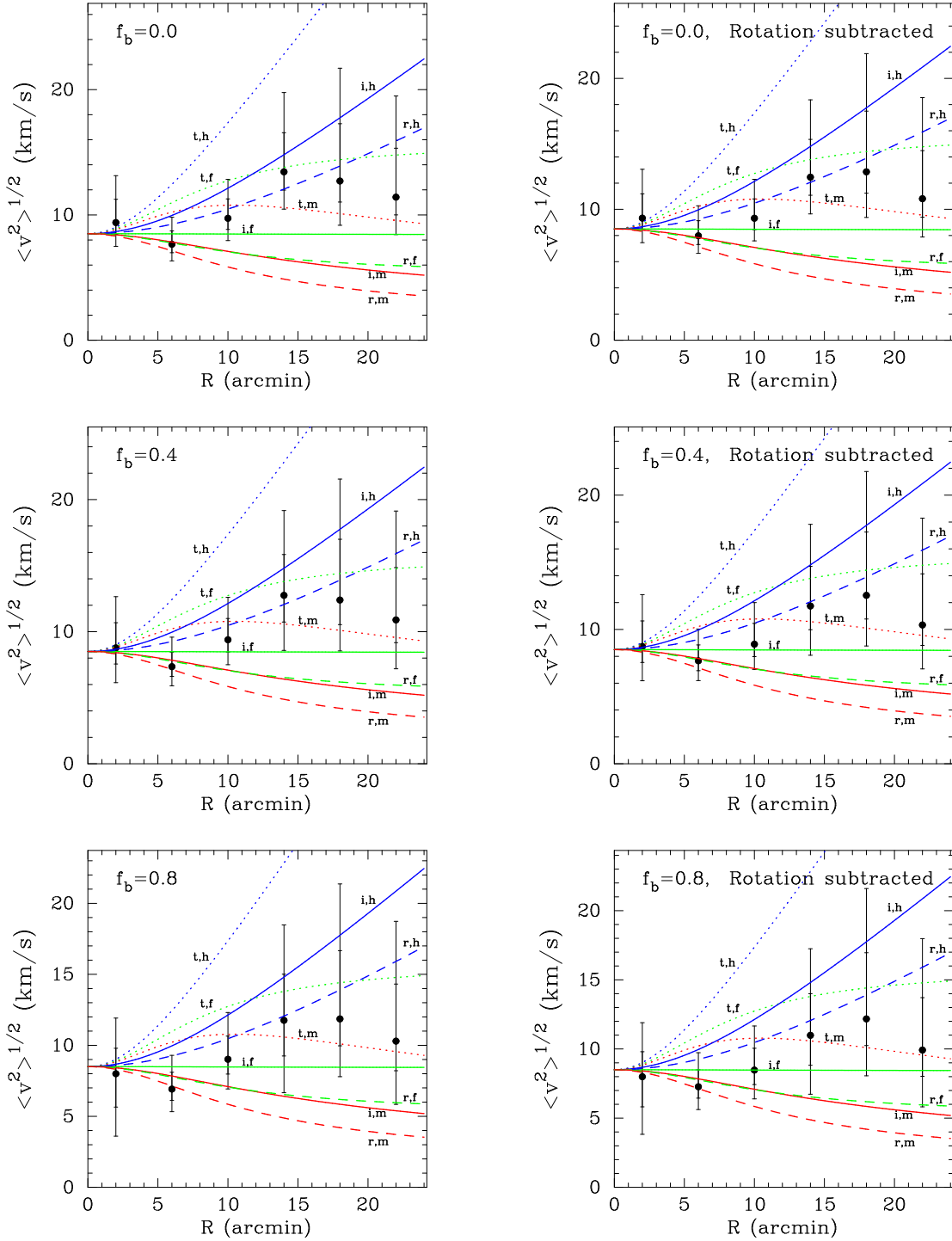


**Figure 7.** Variation of line of sight velocity dispersion with projected radius; Filled circle is the most likely velocity dispersion in each radial bin and the inner and outer error ticks represent 68 and 95 per cent ( $1$  and  $2\sigma$ ) confidence limits respectively. Figures in the left column contain observed velocities; figures in the right column contain velocities with the solid-body rotational component subtracted. From top to bottom, the figures assume an increasing binary fraction  $f_b$ . Binaries are taken from the empirical solar neighbourhood distribution of Duquennoy and Mayor (1991) and are then evolved through circularisation and angular momentum loss, as described in the text. The smooth curves are drawn from the  $\alpha, \gamma$  models of Wilkinson et al. (2001), and the two letter codes denote the model type –  $t$ : tangentially anisotropic ( $\gamma = -6.1$ , or  $\nu = -0.6$ );  $i$ : isotropic ( $\gamma = \nu = 0$ );  $r$ : radially anisotropic ( $\gamma = 1.5$ , or  $\nu = 0.6$ ) –  $h$ : harmonic halo ( $\alpha = -2$ );  $f$ : flat rotation curve halo ( $\alpha = 0$ );  $m$ : mass follows light ( $\alpha = 1$ ). All models are normalised to have a central velocity dispersion of  $8.5 \text{ km s}^{-1}$ , in agreement with the observed value as well as the published value of AOP.

persion for models in which rotation on the sky has been subtracted; we accomplish this subtraction by transforming each velocity  $v_i$  to  $v'_i = v_i - (\xi_x x_i + \xi_y y_i)$ , where the vector  $(\xi_x, \xi_y)$  is computed by requiring the projected angular momentum  $\mathbf{L}$  to equal zero according to

$$\mathbf{L} = (L_x, L_y) = \left( \sum_i v'_i y_i, -\sum_i v'_i x_i \right) = (0, 0). \quad (2)$$

The velocities produced by this rotation subtraction are not necessarily dynamically meaningful because we are also subtracting any genuine rotational component as well as any tidal component. However, the purpose of examining rotation subtracted data is to demonstrate that the observed variation of the velocity dispersion with radius cannot be attributed to tidal effects. Indeed, after rotation subtraction, we will systematically under-estimate the velocity dispersion at large radii because the Gaussian dispersion model to which the data are fit do not include the effects of rotation subtraction on a non-rotating distribution.

Furthermore, Draco will appear to have a perspective induced apparent rotation caused by the variation of the line-of-sight angle across its face (Fest, Thackeray, & Weselink 1961). The solar motion component of this rotation is  $1 \text{ km s}^{-1}$   $30'$  from the centre. The component from Draco's motion is poorly constrained because Draco's proper motion is uncertain. Monte-Carlo orbital simulations of Draco's orbit based on its proper motion show that Draco's most probable line-of-sight angle is  $70^\circ$ , implying a perspective rotation of  $2.5 \text{ km s}^{-1}$  across  $30'$ . However, this rotation increases to  $5 \text{ km s}^{-1}$  if the line-of-sight angle is  $80^\circ$ . Analysing Draco's velocities with all rotation subtracted effectively demonstrates that these uncertainties do not affect our dynamical conclusions.

From Figure 7, it is apparent that the velocity rises from the central value of  $8.5 \text{ km s}^{-1}$ . In the most plausible case of no rotation subtraction and a 40 per cent evolved binary fraction, the last three bins have a velocity dispersion larger than the central value with  $1\sigma$ ,  $2\sigma$ , and  $1\sigma$  statistical strengths, with a combined probability  $< 10^{-3}$ . Only when an implausibly large 80 per cent evolved binary fraction is combined with rotation subtraction does this conclusion come under question; however, this large binary fraction is ruled out by the good agreement of our velocities with 61 prior velocities of AOP.

In Figure 8, we plot the variation of the velocity dispersion with projected radius for a subsample of stars with high-quality spectra (Tonry & Davis  $R_{\text{TD}} > 5$  and 7). The  $R_{\text{TD}} > 5$  sample contains 95 stars, and the  $R_{\text{TD}} > 7$  sample contains 73 stars. In neither case does the exclusion of low-quality spectra affect the finding of a rising velocity dispersion.

In the  $R_{\text{TD}} > 7$  panel of Figure 8, the velocity dispersion falls to  $4 \text{ km s}^{-1}$  in first bin, which extends from the centre to  $R = 4'$ . This effect is not the result of sample size effects, because there are 16 stars in this bin, and because our dispersion estimator is valid for small samples. A bootstrap resampling of 16 stars from the 23 stars in the left  $R_{\text{TD}} > 5$  panel of Figure 8 shows that the observed dispersion drop occurs by chance 3 per cent of the time; if the binary fraction is doubled from the 40 per cent fraction assumed, this probability rises to 18 per cent. Given that there

are six radial bins in which such a drop could have been observed, the drop is probably a statistical artefact, and is not the result of the difference in spectrum quality between the two panels.

## 5.2 Direction and Significance of Rotation

When subtracting solid-body rotation from our data set, we found that Draco is rotating at  $6 \text{ km s}^{-1}$  at  $30'$  about an axis with a position angle (PA) of  $62^\circ$  east from north with the northwest side of the galaxy receding. Applying a Monte-Carlo analysis of the proper motion data of Scholz & Irwin (1994), we find that the PA of Draco's proper motion is  $29^\circ_{-19}^{+17}$  in the frame moving with the sun. Thus the perspective induced rotation axis should have a PA of  $119^\circ_{-19}^{+17}$ . This is in  $57^\circ$  or  $3\sigma$  disagreement with the observed rotation axis.

Corrected for solar motion, Draco's proper motion vector has a PA of  $42^\circ_{-23}^{+23}$ . This is in  $2\sigma$  disagreement with the PA of the major axis of Draco at  $88^\circ_{-3}^{+3}$  (Odenkirechen et al. 2001), arguing against tidal stretching. Additionally, the axis of tidally induced rotation should have a PA of  $132^\circ_{-23}^{+23}$  because it is expected to be perpendicular to the motion (eg. Oh, Lin, & Aarseth 1995); this is in  $70^\circ$  or  $3\sigma$  disagreement with the observed rotation axis angle of  $62^\circ$ .

Additionally, we performed a Monte Carlo simulation to test the significance of the rotation observed in our Draco data, modelling it as drawn from a  $10 \text{ km s}^{-1}$  non-rotating Gaussian distribution. We found that 5 per cent of the time, this non-rotating distribution had  $\mathbf{L}$  larger than that observed in the actual data. We also performed a more realistic simulation with stars drawn from a non-rotating Gaussian possessing the observed radial dispersion variation, and included binary contamination with a 40 per cent unevolved binary population. For this simulation, the probability of randomly seeing an equal or larger rotation is 14 per cent.

In summary, the rotation we observe is statistically weak, inconsistent with tides, and inconsistent with the perspective effect. Furthermore, the elongation of Draco is misaligned with Draco's proper motion at the  $1.7\sigma$  level. Thus there is no evidence of tidal effects in our Draco data, or in the proper motion data of Scholz & Irwin (1994). This is in agreement with the absence of tidal truncation noted in SDSS Draco data (Odenkirechen et al. 2001).

The direction of our observed rotation is inconsistent with the finding of AOP, who found rotation about an axis with a position angle of  $15^\circ$  at the  $1\sigma$  significance level. However, Hargreaves et.al. (1996) also found  $2\sigma$  rotation about the major axis though from a centrally concentrated sample of 17 stars. None of these findings are statistically significant enough to constitute a genuine detection of rotation.

## 5.3 Model Fitting

In Paper I, we introduced a set of two parameter dynamical models for spherical stellar systems. These models are designed to probe the principal observational degeneracy – namely, the trade-off between halo mass and orbital anisotropy. For example, a dSph like Draco, with large velocities at extended projected radii, may have either a large dark matter halo or may have orbits that are tangentially anisotropic. In the latter case, the large apparent velocity

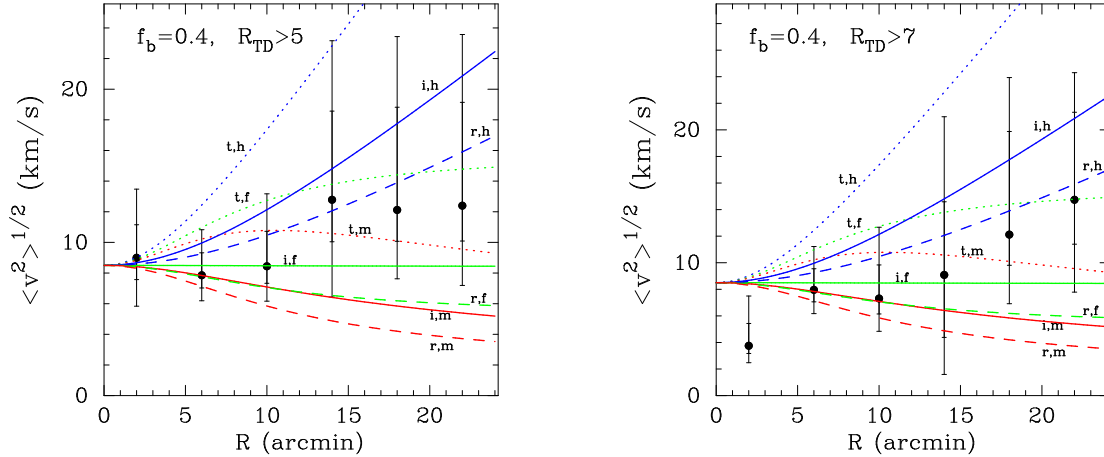


**Figure 8.** Variation of line-of-sight velocity dispersion for good quality spectra with a comparatively large Tonry & Davis (1979)  $R_{TD}$  value. Left:  $R_{TD} > 5$ ; Right:  $R_{TD} > 7$ .

dispersion arises from the fact that, at large radii, the radial velocities observed are drawn in large part from circular orbits viewed edge-on.

The two parameters of the models are  $\alpha$ , which determines the dark matter content and  $\gamma$ , which determines the velocity anisotropy. An  $\alpha = 1$  model corresponds to a mass-follows-light dSph;  $\alpha = 0$  is a dSph with a flat rotation curve; and  $\alpha = -2$  is the case of a dSph immersed in the centre of a uniform density (harmonic) halo. When  $\gamma = 2$ , the orbits are radial at large radii. When  $\gamma = 0$ , the velocity distribution is isotropic (as is a King model). When  $\gamma = -\infty$ , the orbits are all circular at large radii. The light distribution of these models is independent of the potential and is always represented by a Plummer (1911) model. As shown in Paper I, a Plummer model with a core radius  $r_0 = 9.7'$  is a good fit to Draco's stellar surface density – as good as the King models that are customarily used.

Our method of fitting the data is identical to the method used for the synthetic datasets of Paper I. In summary, a line profile is derived from the model by numerically integrating out the tangential velocities. This line profile is tabulated in a multi-dimensional spline table. This allows rapid generation of the line-of-sight velocity ( $v_{los}$ ) line profile  $L(v_{los}, R; \alpha, \gamma)$  for any value of projected radius  $R$  and  $\alpha, \gamma$ . The line profile is then convolved with a binary distribution and Gaussian velocity measurement uncertainty profile  $\sigma$  to give  $\tilde{L}(v_{los}, R, \sigma; \alpha, \gamma)$ . The probability of observing an ensemble of points at  $R_i$  with velocity and velocity uncertainty  $v_i, \sigma_i$  is

$$P(\{R_i, v_i, \sigma_i\} | \alpha, \gamma) = \prod_i \tilde{L}(v_i, R_i, \sigma_i; \alpha, \gamma) \quad (2)$$

Finally,  $P(\{R_i, v_i, \sigma_i\} | \alpha, \gamma)$  is tabulated over a grid of  $\alpha, \gamma$ , and the resulting likelihood contours and their projections onto the  $\alpha, \gamma$  axes are used to constrain the best-fit  $\alpha, \gamma$ .

Figure 9 shows the result of fitting our Draco velocity data with the two-parameter dynamical model for various combinations of binary fraction and rotation-subtraction. The fits are presented as likelihood contours in the two-dimensional parameter space of the model. Here, we have symmetrised the  $\gamma$  parameter describing the anisotropy by defin-

ing a new anisotropy parameter  $\nu = -\log_{10} [(2 - \gamma) / 2]$ . The value  $\nu = 1$  then corresponds to a system in which  $\langle v_r^2 \rangle / \langle v_\theta^2 \rangle \rightarrow 10$  in the limit of large radii;  $\nu = 0$  is isotropic; and  $\nu = -1$  corresponds to a system in which  $\langle v_r^2 \rangle / \langle v_\theta^2 \rangle \rightarrow 1/10$ . The left panels use the observed data, and the right panels use rotation subtracted data. In all instances, including the extreme case of rotation-subtracted data and a 0.6 evolved binary fraction, a mass-follows-light model ( $\alpha = 1$ ) is ruled out at the 2 to 3 $\sigma$  level. Likewise, in all cases, an extended halo with a harmonic core ( $\alpha = -2$ ) is ruled out at the 2 to 3 $\sigma$  level.

Assuming a 40 per cent binary fraction and omitting rotation subtraction produces the best fit values  $\alpha = -0.34$ , and  $\nu = -0.18$  in two dimensions. For the projected (one-dimensional) distributions, the median values are  $\alpha = -0.26$  with a  $1\sigma$  range -0.78 to 0.25, and  $\nu = -0.22$  with a  $1\sigma$  range -0.39 to -0.05. These values correspond to a dSph with a weakly tangentially anisotropic distribution of velocities. At large radii, the velocity dispersions have the property  $\langle v_r^2 \rangle / \langle v_\theta^2 \rangle \rightarrow 0.56$ . The dark matter is distributed in a nearly isothermal halo. More exactly, the rotation curve of the halo is very slowly rising like  $r^{0.17}$  at large radii. Extremely anisotropic velocity distributions, as well as halo models markedly deviating from isothermal, are ruled out.

Figure 10 checks the robustness of our maximum likelihood solution against possible errors. The dataset is now analysed with an assumed luminous Plummer core radius 20 per cent larger than the best-fit value (top), or assuming that the velocity uncertainties have been underestimated by a factor of  $\sim 2$  (centre), or with an assumed central velocity dispersion of  $10 \text{ km s}^{-1}$  (bottom). In all cases, the maximum likelihood solution barely changes. The fact that a large mis-estimation of the Plummer core radius does not affect the result strongly suggests that the exact form of the parameterised stellar density is not important.

Finally, Figure 11 shows the results of performing the model fit with good quality spectra only. Although the contours are considerably broader than before, the  $\alpha = 1$  mass-follows-light model is ruled out at a comparable statistical significance. The most likely model has a somewhat more massive halo and is less isotropic than when the fit was per-

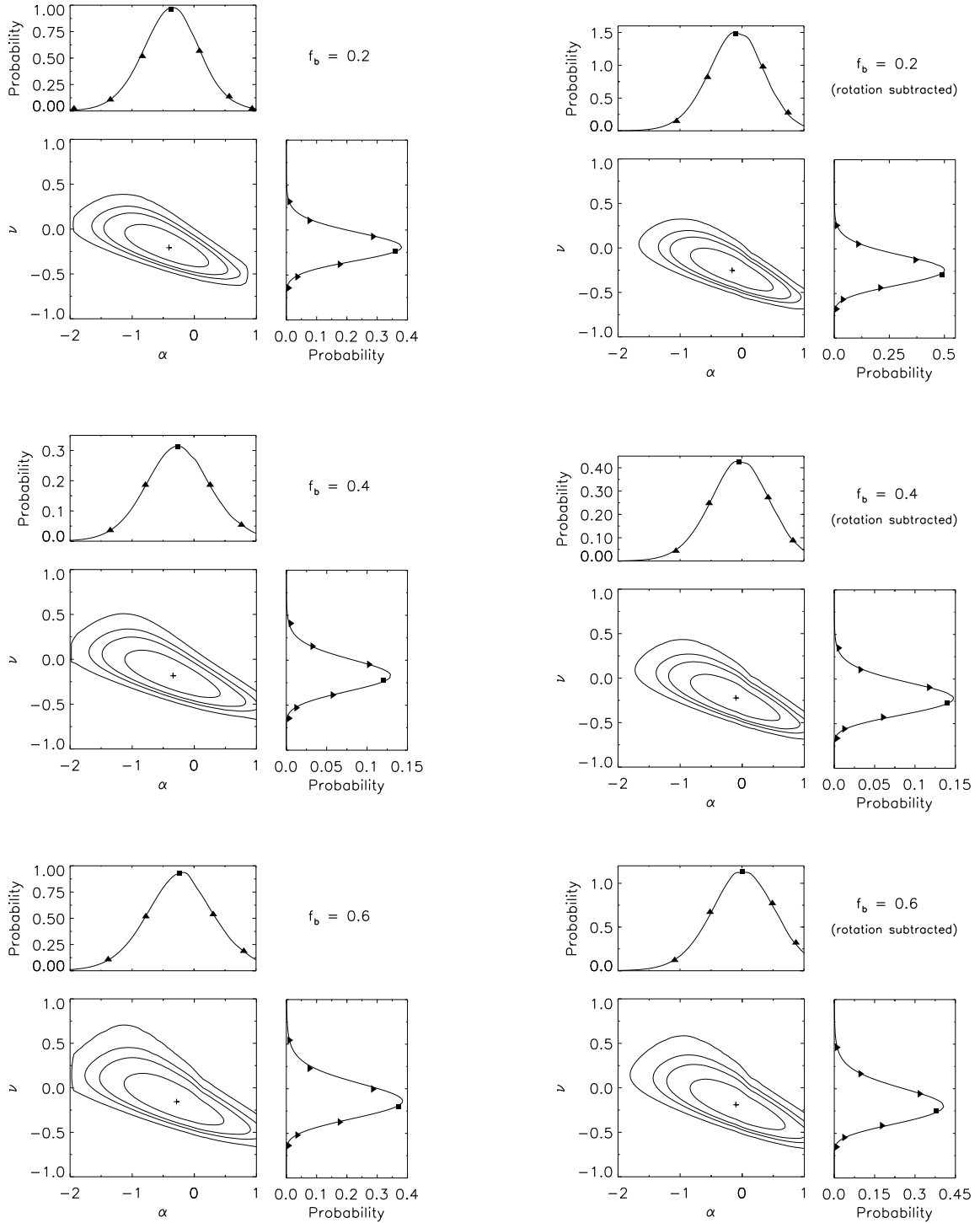


**Figure 9.** Likelihood contours of the fit of our Draco data to the two-parameter  $\alpha, \gamma$  models of Wilkinson et al. (2001);  $\nu = -\log_{10} [(2 - \gamma)/2]$  is used as a symmetrical surrogate for the anisotropy parameter  $\gamma$ . The contours are at enclosed two-dimensional  $\chi^2$  probabilities of 0.68, 0.90, 0.95, and 0.997. The top and right panels of each plot represent the probability distributions of  $\alpha$  and  $\nu$ , respectively; the median of each distribution is represented by a square, and the triangles are at 0.68, 0.95, and 0.997 enclosed probabilities.  $f_b$  is the binary fraction used, assuming evolved binaries, as described in the text. The left column contains analyses of the data as observed; the right column uses data from which the rotational component of motion has been subtracted.

formed with the entire sample. However, the two fits are consistent well within the  $1\sigma$  level. Hence it is quite unlikely that our finding of a largely isotropic distribution function inside an extended halo is the result of velocity errors in

low-quality spectra.

From the best-fit  $\alpha, \nu$  values of Figure 9, it is possible to constrain Draco's mass-to-light ratio, at least within the region in which data exist. For a typical  $\alpha = -0.3, \nu =$

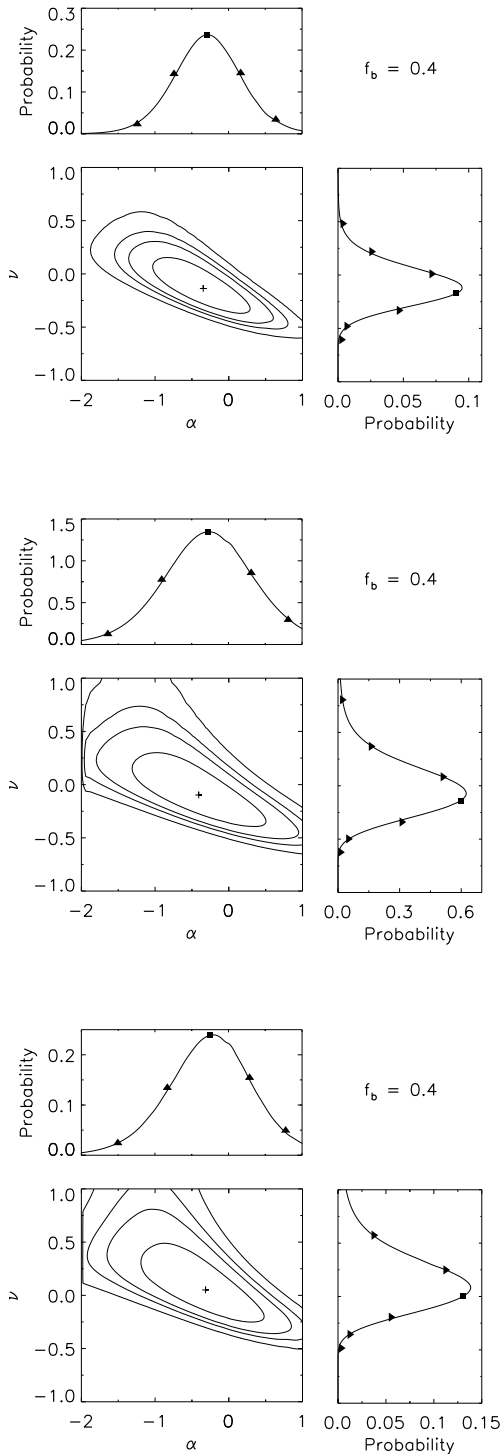


**Figure 10.** The model fits of Figure 9 repeated with the introduction of deliberate errors. Top: The Plummer core radius of the light has been increased by 20 per cent over the best-fit value. Centre: The velocity uncertainties have been increased by a factor of  $\sim 2$  by setting all velocity uncertainties less than  $2 \text{ km s}^{-1}$  equal to  $4 \text{ km s}^{-1}$ . Bottom: The central velocity dispersion of the model has been set to  $10 \text{ km s}^{-1}$ , rather than the observed value of  $8.5 \text{ km s}^{-1}$ .

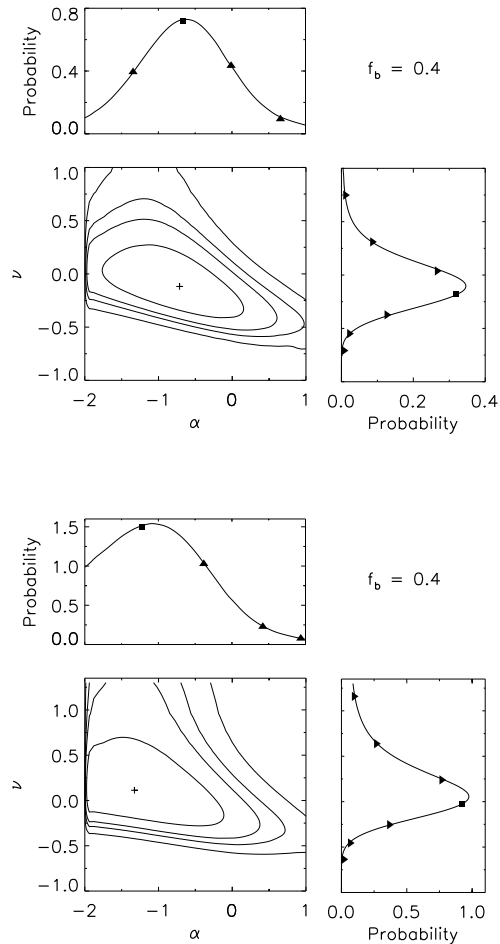


**Figure 11.** The model fits of Figure 9 repeated using stars with good quality spectra only. Top: spectra with Tonry & Davis  $R_{\text{TD}} > 5$ ; Bottom: spectra with Tonry & Davis  $R_{\text{TD}} > 7$ .

$-0.25$  best-fit model, the mass within three core radii is  $8_{-2}^{+3} \times 10^7 M_{\odot}$ . The mean mass-to-light ratio within 3 core radii is  $(330 \pm 125) M_{\odot} / L_{\odot}$ , assuming a luminosity of  $(2.4 \pm 0.5) \times 10^5 L_{\odot}$  (Odenkirchen et.al. 2001). Although our mass superficially appears consistent with AOP (1995) and Hargreaves et.al. the mass we measure is actually the inner part of a halo, rather than the total mass of a mass-follows-light distribution.

## 6 CONCLUSIONS

We have carried out a radial velocity survey of the Draco dwarf spheroidal (dSph) galaxy using the AF2/WYFFOS instrument at the William Herschel Telescope. A total of 284 stars were targeted. Of these, 203 stars had usable velocities, 186 stars turned out to be Draco members and 159 stars had velocities of sufficient quality for our subsequent dynamics analyses. As our initial target list was based on accurate CCD data, rather than photographic plate photometry, we achieved a clean separation between Draco's giant branch population and the Galactic foreground out to the tidal radius. Consequently, our dataset contains many more stars at large radii than previous studies. We calibrated the measurement uncertainties of our dataset by subdividing the

bright stars into two velocity measurements, and using the discrepancies between the measurements to rescale the nominal IRAF Tonry-Davis  $R$  value errors. Our final mean and median velocity uncertainties were approximately  $2 \text{ km s}^{-1}$ .

By chance, 62 of our stars were also contained in the prior set of Armandroff, Olszewski & Pryor (1995, AOP). These stars were in good  $\chi^2$  agreement with our own measurements, confirming the validity of our uncertainty estimates. Furthermore, the good agreement between the two datasets argues against the earlier claim by AOP that Draco possesses an extraordinarily large binary fraction because the excess binaries would have inflated the  $\chi^2$  disparity between the two datasets more than was observed. In fact, the datasets are completely consistent with a binary distribution and fraction comparable to those in the solar neighbourhood.

These new data allow – for the first time – a robust measurement of the variation of the velocity dispersion with projected radius. Hints of a variation have been noted by previous authors (Hargreaves et al. 1996), but at much lower statistical significance. We have shown that the velocity dispersion of Draco’s stars increases with increasing radius. This provides the first direct evidence for the existence of an extended halo in any dSph. The rise of the velocity dispersion is robust against changes in the assumed binary fraction, measurement errors and the subtracted solid body rotation.

The new dataset warrants a more sophisticated approach to dynamical modelling than has been customary before. We have used the two parameter family of spherical models introduced by Wilkinson et al. (2001, Paper I), for which the projected density provides a good match to the starcount data. The first parameter is the velocity anisotropy of the stars, the second parameter is the dark matter content. The models project to the same surface density on the sky, but the dark matter content can vary between the extremes of mass-follows-light and an extended dark halo with a harmonic core. Similarly, the velocity can vary from the circular orbit model through isotropy to the radial orbit model. The fit implements our novel maximum likelihood algorithm, which makes proper allowance for the effects of measurement errors and contamination by binary stars in the radial velocity dataset.

Draco is best fit by a slightly tangentially anisotropic orbital distribution and with a halo that falls off somewhat more slowly than a flat rotation curve model. We are able to rule out both a mass-follows-light model and an extended halo with harmonic core at the  $3\sigma$  significance level (subject only to the limitations of our parameterised models). These conclusions are largely independent of the assumed binary fraction and are insensitive to the subtraction of solid body rotation. This provides the first definitive evidence that the mass-to-light ratio increases outwards and that the dark matter in Draco resides in a near-isothermal halo.

Our success in eliminating the systematic effects of the strong sky lines in the region of the Ca triplet demonstrates that we have not approached a fundamental limiting magnitude and that a 4m telescope (like the WHT) should be capable of observing stars much fainter along the giant branch in Draco. The strong rise of the luminosity function with magnitude implies that even a modest increase in limiting magnitude will provide a much larger sample of stars for dynamical modelling. For instance, we estimate that extending

the magnitude limit to  $V \sim 20.5$  will increase the sample size by a factor of three or so. In other words, datasets of  $\sim 600$  discrete radial velocities in Draco are easily within the grasp of current technology. We conclude that future prospects for mapping out the detailed distribution of dark matter in Draco with stellar kinematics are excellent.

## ACKNOWLEDGMENTS

MIW and JK acknowledge financial support from PPARC, while NWE thanks the Royal Society. We thank Chris Tout for helpful suggestions on the modelling of giant branch binary evolution, and the anonymous referee for useful comments and suggestions. We also thank Colin Frayn for his help in acquiring the Draco velocity data.

## REFERENCES

- Aaronson M., 1983, ApJ, 266, L11  
 Aaronson M., Olszewski E.W., 1987, in “Dark Matter in the Universe” (IAU Symposium No. 117), eds J. Kormendy, G.R. Knapp, (Reidel, Dordrecht), p. 153  
 Aaronson M., Olszewski E.W., 1988, in “Large Scale Structures of the Universe” (IAU Symposium No. 130), eds J. Audouze, M.C. Pelletan, A. Szalay, (Kluwer, Dordrecht), p. 153  
 Armandroff T.E., Olszewski E.W., Pryor C. 1995, AJ, 110, 2131 (AOP)  
 Binney J., Tremaine S. 1987, Galactic Dynamics, (Princeton University Press, Princeton)  
 Duquennoy A., Mayor M., 1991, MNRAS, 248, 485 (DM)  
 Feast, M.W., Thackeray, A.D., Wesselink, A.J., 1961, MNRAS, 122, 433  
 Hargreaves J.C., Gilmore G., Irwin M.J., Carter D., 1996, MNRAS, 282, 305  
 Hargreaves J.C., Gilmore G., Annan J.D., 116, MNRAS, 279, 108  
 Hurley J., Tout C., Pols, P., 2001, MNRAS, submitted  
 Irwin M., Hatzidimitriou D. 1995, MNRAS, 277, 1354  
 Lokas, E.L., 2001, MRAS, accepted, astro-ph/0107479  
 Oh K.S., Lin D.N.C., Aarseth S.J., 1995, ApJ, 442, 142  
 Odenkirchen M., et al. 2001, AJ, astro-ph/0108100  
 Olszewski E.W., Pryor C., Armandroff T.E., 1996, AJ, 111, 750  
 Plummer H.C. 1911, MNRAS, 71, 460  
 Scholz R.-D., Irwin M.J., 1994, in “Astronomy from Wide Field Imaging (IAU Symposium 161), ed H.T. McGillivray et al. (Kluwer, Dordrecht), p. 535  
 Tonry J., Davis M. 1979, AJ, 84, 1511  
 Wilkinson M.I., Kleyana J., Evans N.W., Gilmore G., 2001, MNRAS, submitted (Paper I)  
 Wyse R., Gilmore G., 1992, MNRAS, 257, 1

This paper has been produced using the Royal Astronomical Society/Blackwell Science  $\text{\TeX}$  macros.